



Detection and Localization of F-layer Ionospheric Irregularities with Back Propagation Method Along Radio Occultation Ray Path

Vinícius Ludwig-Barbosa¹, Joel Rasch², Thomas Sievert¹, Anders Carlström³, Mats I. Pettersson¹, Viet Thuy Vu¹, and Jacob Christensen³

¹Blekinge Institute of Technology, Karlskrona, Sweden

²Molflow, Gothenburg, Sweden

³RUAG Space AB, Gothenburg, Sweden

Correspondence: Vinícius Ludwig-Barbosa (vinicius.ludwig.barbosa@bth.se)

Abstract. The back propagation (BP) method consists of diffractive integrals computed over a trajectory path, projecting a signal to different planes. It unwinds the diffraction and multipath, resulting in minimum disturbance on the BP amplitude when the auxiliary plane coincides with the region causing the diffraction. The method has been previously applied in GNSS Radio Occultation (RO) measurements showing promising results in the location estimate of ionospheric irregularities but without complementary data to validate the estimation. In this study, we investigate with wave optics propagator (WOP) simulations of an equatorial C/NOFS occultation with scintillation signatures caused by an equatorial plasma bubble (EPB), which was parametrized with aid of collocated data. In addition, a few more test cases were designed to assess the BP method regarding size, intensity and placement of single and multiple irregularity regions. The results show a location estimate accuracy of 10 km (single bubble, reference case), where in multiple bubble scenarios only the strongest disturbance would be resolved properly. The minimum detectable disturbance level and the estimation accuracy depend on the receiver noise level, and in the case of several bubbles on the distance between them. The remarks of the evaluation supported the interpretation of results for two COSMIC occultations.

1 Introduction

The Fresnel-Huygens' method consists of the propagation in vacuum of a complex wave by computing a diffractive integral of the electromagnetic (EM) field over a plane to one or multiple points in space (Sommerfeld, 1967). The direct form of the line integral is extensively combined with wave optics propagator (WOP) (Knepp, 1983) in order to obtain the EM field equivalent to the GNSS complex signal sampled on the LEO orbit after sounding the Earth's atmosphere during a radio occultation (RO) event (Bevis et al., 1992; Kursinski et al., 1997; Gorbunov and Lauritsen, 2007).

The inverse problem, from LEO orbit to a desired plane or phase screen (PS), has been investigated in order to disentangle the multipath and the diffraction from the received total field and to increase the resolution of the bending angle inversion in the lower atmosphere. (Gorbunov and Gurvich, 1998a, b; Dahl Mortensen, 1998). The regions with sharp gradients in refractivity, i.e. non-homogeneities, are the source of diffraction and multipath in amplitude and phase during the forward propagation, according to the Huygens' principle (Sommerfeld, 1967). The inverse form of the diffractive integral, hereafter



back propagation (BP) method, computes the projection of the complex signal to BP planes in the atmosphere. Ideally, the
25 disturbance observed in the BP amplitude are the lowest at the BP plane matching the placement of the irregularity region. The
back propagation field is not fully comparable to the forward field since the back projection is performed in vacuum, i.e. the
impact height on the initial plane (boundary condition) is prolonged as straight lines to each BP plane (Gorbunov and Gurvich,
1998a).

The GNSS signal also experiences multipath and diffraction during the ionospheric propagation, where plasma irregulari-
30 ties above ~ 80 km altitude are responsible for rapid fluctuations in amplitude and phase, known as ionospheric scintillation
(Aarons, 1982; Yeh and Liu, 1982; Wickert et al., 2004). In the E-layer (~ 90 – 130 km), the regions have enhanced electron
density due to concentration of metallic ions driven by wind shear, with main occurrence in mid-latitudes and during summer
(Arras and Wickert, 2018). In the F-layer, the irregularity regions in low latitudes are commonly referred to as Equatorial
Plasma Bubbles (EPB) or Equatorial Spread F (ESF). The phenomenon is driven by the Rayleigh-Taylor instability mechanism
35 with higher occurrence on post-sunset hours (local time), where the recombination of ions in the low altitude creates vertical
gradient in the plasma density extending upwards to the F-region. A natural flow from the less dense (low altitudes) to denser
regions (high altitudes) creates depletion areas in the form of plumes (Kelley et al., 1981; Stolle et al., 2006). The higher turbu-
lence and gradient in density on the edges of the up-flowing bubble distorts the EM wave and eventually creates disruption in
the operation of RF systems (Kelly et al., 2014). The irregularities are observed in different scale sizes (Xiong et al., 2016) and
40 the occurrence of EPB has shown significant seasonal, solar cycle and activity dependence (Stolle et al., 2006, 2008; Kepkar
et al., 2020). In high latitudes, the occurrence of irregularity regions are not restricted by local time and are mostly originated
by particle precipitation triggered by geomagnetic activities (Jiao and Morton, 2015).

Following the same principle as in the lower atmosphere, the location of ionospheric irregularities in E- and F-layer has
been estimated with BP method along the RO ray path (Gorbunov et al., 2002; Sokolovskiy et al., 2002; Cherniak et al.,
45 2019). Back propagation has been applied to real measurements but the estimate accuracy has been primarily assessed with
WOP simulation of a generic occultation event, including a single iso- or anisotropic irregularity region modelled by one or
multiple phase screens (Sokolovskiy et al., 2002). Thus far, the location of irregularities patches is not self-reliant based solely
in occultation measurements given the characteristics of the technique, namely the long separation between GPS and LEO
satellite and the sampling in a 1-D trajectory. The opportunity of occultation events collocated to independent techniques must
50 be taken to further evaluate the capabilities of the BP method in RO measurements. In Carrano et al. (2011), the scintillation
pattern observed in an occultation performed by C/NOFS (Communications/Navigation Outage Forecasting System) satellite
and caused by a plasma bubble was fully modelled thanks to the parametrization of the disturbance assisted by collocated data,
being the bubble – LEO satellite distance an important variable.

In our study, the BP method is further assessed with WOP simulations to determine its capabilities and limitations in the
55 context of detection and location of F-layer irregularity regions, i.e., plasma bubbles, in RO measurements. The modelling
described in Carrano et al. (2011) is considered as the initial assessment scenario of a plasma bubble in F-region along the ray
path and it was used to design a few more cases with different placements, sizes, fluctuation intensities and number of regions.
Sect. 2 introduces the concept of back propagation and its equations in the scenario of an occultation event. Sect. 3 describes



the modelling of the ionosphere and plasma bubbles in WOP simulations. Additionally, it addresses the test cases considered in our evaluation. The simulations results are discussed in Sect. 4 and support the interpretation of two COSMIC (Constellation Observing System for Meteorology, Ionosphere, and Climate) measurements reported in Cherniak et al. (2019). Finally, the conclusions of the study are summarized in Sect. 5.

2 Back propagation

Assuming the scenario of a RO simulation, the last stage of a wave optics propagator (WOP) takes place in a region that can be approximated to vacuum. Therefore, the projection of the total field in LEO orbit can be computed by the following diffraction integral (Sommerfeld, 1967),

$$u_o(x, y) = \sqrt{\frac{k}{2\pi}} \int u(x, y) \cos \xi \frac{\exp(ik|\mathbf{r} - \mathbf{r}_o| - i\pi/4)}{|\mathbf{r} - \mathbf{r}_o|^{1/2}} dS, \quad (1)$$

where u is the total field at the last phase screen (PS), k is the wavenumber, ξ is the angle formed by the normal vector to the integration plane (\hat{N}) and $\mathbf{r} - \mathbf{r}_o$, and dS is set by dy for the case of a vertical plane. Figure 1 shows the RO geometry considered in the computation of the diffraction propagation, where the origin of the coordinate system is the Earth's center, viz $|\mathbf{r} - \mathbf{r}_o| = ([x - x_0]^2 + [y - y_0]^2)^{1/2}$.

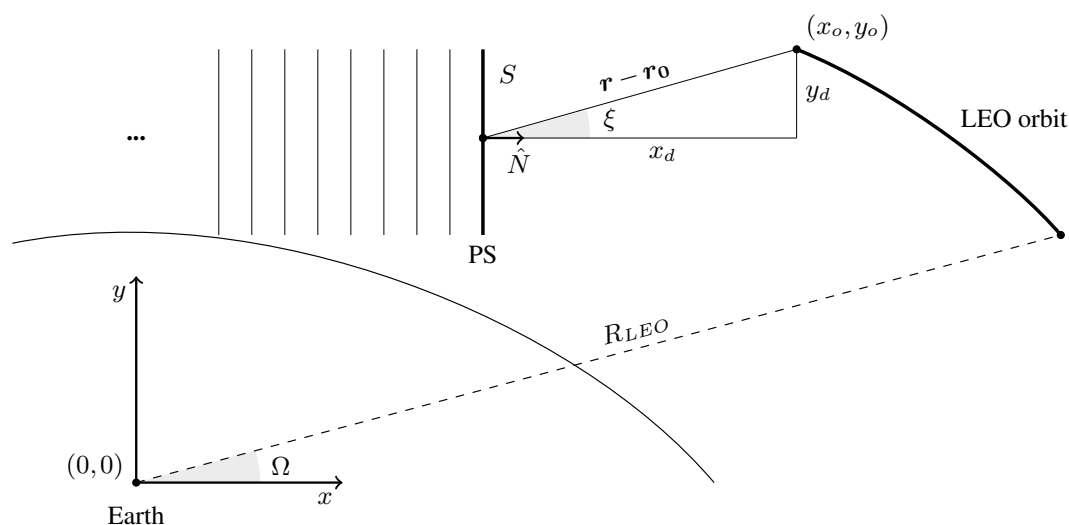


Figure 1. Diffraction propagation geometry.

Applying the same principle, it is possible to calculate the total field backwards to the last screen or any screen from $u(x_o, y_o)$ under the assumption of vacuum propagation. Therefore, the diffraction integral for the propagation in the opposite direction



is written as

$$75 \quad u_b(x, y) = \sqrt{\frac{k}{2\pi}} \int u_o(x, y) \cos \xi \frac{\exp(-ik|\mathbf{r} - \mathbf{r}_b| + i\pi/4)}{|\mathbf{r} - \mathbf{r}_b|^{1/2}} dS. \quad (2)$$

However, the integration line (LEO orbit) is not a vertical plane like the phase screen. If we assume R_{LEO} as the orbit radius for the LEO satellite, then $dS = R_{LEO} d\Omega$.

The angle ξ is now the angle formed by vector $\mathbf{r} - \mathbf{r}_o$ and the normal vector to the LEO orbit at a given coordinate (x_b, y_b) . Figure 2 shows the geometry of the back propagation problem, the relation between the angles and the normal vector direction changing along the LEO orbit.

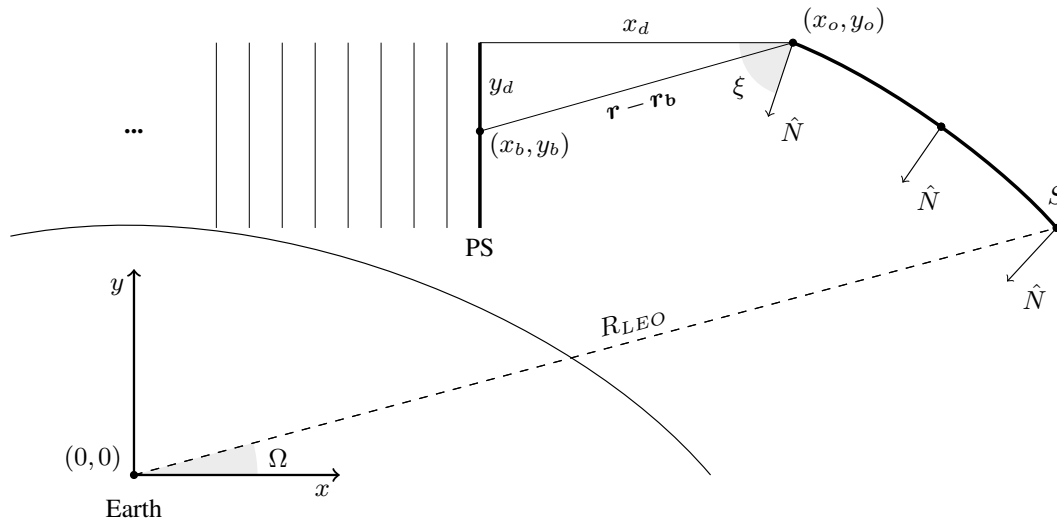


Figure 2. Back propagation geometry.

80 The general equation for the normal vector along the curved path is defined as

$$\hat{\mathbf{N}} = -\cos \Omega \hat{x} - \sin \Omega \hat{y}, \quad (3)$$

and $\cos \xi = \hat{\mathbf{N}} \cdot \hat{\mathbf{r}}$. Thus, the final expression for (2), which in this format is suitable for real LEO orbits, is therefore given by

$$u_b(x, y) = \sqrt{\frac{k}{2\pi}} \int u_o(x, y) \hat{\mathbf{N}} \cdot \hat{\mathbf{r}} \frac{\exp(-ik|\mathbf{r} - \mathbf{r}_{BP}| + i\pi/4)}{|\mathbf{r} - \mathbf{r}_{BP}|^{1/2}} R_{LEO} d\Omega. \quad (4)$$

85 Slightly different procedures are described in the literature to obtain the total field at multiple parallel BP planes: 1. (4) can be computed to obtain the BP amplitude at different vertical planes (Sokolovskiy et al., 2002) or 2. direct and inverse Fourier transforms can be repeated recursively, assuming the BP signal at the right-most PS in Fig. 2 as the initial boundary condition,

$$\tilde{u}_b(x_b, k_y) = \mathfrak{F}\{u_b(x_b, y_b)\}, \quad (5)$$

$$u_b(x, y) = \mathfrak{F}^{-1}\left\{\tilde{u}_b(x_b, k_y) \exp\left(i\sqrt{k^2 - k_y^2}(x - x_b)\right)\right\}, \quad (6)$$



90 where \mathfrak{F} is the Fourier operator and k_y is the spatial angular frequency. The second approach is referred to as Zverev transform (Gorbunov et al., 2002; Gorbunov and Lauritsen, 2007).

The overall procedure to estimate the distance from the irregularity patch to the LEO satellite relies on finding the auxiliary plane with the minimum standard deviation BP amplitude (σ_u). The boundary condition of the BP method is the total field sampled on the LEO orbit, which corresponds to the superposition of a primary and a secondary field. The primary is radiated
95 from the GNSS satellite whereas the secondary results from the vibration of ions as the primary field moves through the ionosphere. Within the bubble region, the wave field is propagated through sharp gradients in electron density. That creates nonhomogeneous advances in phase, viz phase velocity $v_p = c/n_i$ being the ratio between speed of light in vacuum and ionospheric refractive index, $n_i < 1$ around F-layer (Culverwell and Healy, 2015). As a result, rapid variations in amplitude and phase will lead to interference in the total field (focusing and defocusing), i.e scintillation (Yeh and Liu, 1982). The ability
100 of finding the origin of the secondary field along the ray path is dependent on the secondary field amplitude (proportional to the electron density), and on the noise level of the LEO receiver. Figure 3 illustrates the interplay of focusing and defocusing yielded by the electron density gradient, represented in terms of refractive index (n), within the irregularity patch and the resultant total field in the observational plane (last phase screen).

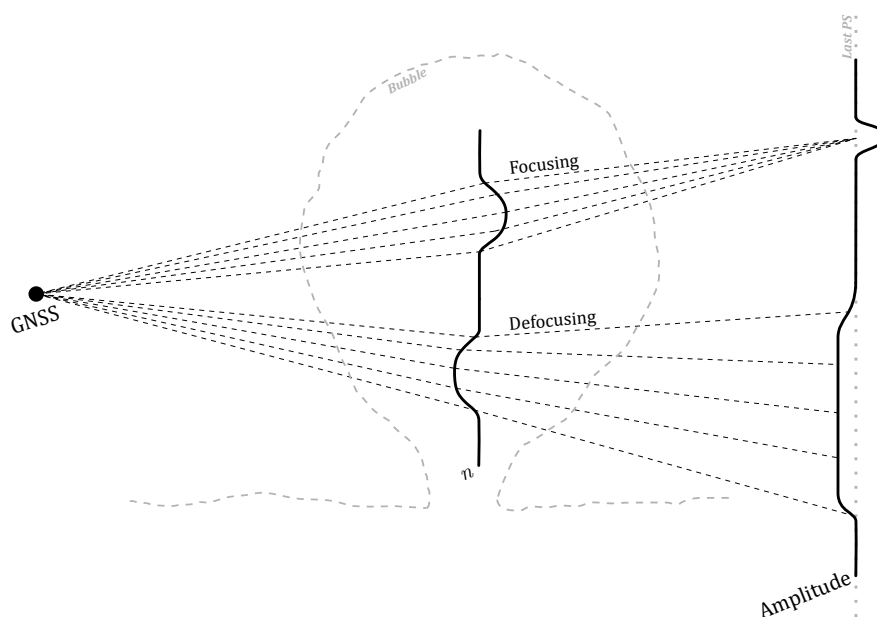


Figure 3. Illustration of the wave field generated on the GNSS transmitter (primary field); the ionospheric mechanisms triggered by the secondary field due to the vibration of ions; followed by the overall expansion of the wave field until the observation plane (last phase screen).



3 Ionospheric simulation

105 The effects of ionospheric refractivity are accounted in a WOP simulation by assuming the electron density profile (EDP) as part of the atmospheric model. The refractive index combines neutral atmosphere and ionosphere is defined as

$$n_i = -40.3 \frac{\rho}{f^2}, \quad (7)$$

$$n = n_n + n_i, \quad (8)$$

110 where f is the carrier frequency, ρ is the electron density (el/m^3), and subscripts n and i denote the neutral atmosphere and ionosphere, respectively. The addition of the ionospheric model includes the respective phase shift into the total phase accumulated during the wave propagation. In RO perspective, the excess path due to the ionospheric propagation under such a scenario may result in an extra accumulated bending angle which is proportional to f^{-2} which means the signals in different frequencies are going to have different bending angles, due to slightly different propagation paths. Consequently, they have different integrated electron density, $\int \rho ds$, where lower the frequency, larger the bending (Culverwell and Healy, 2015).

115 3.1 F-region irregularity: Plasma bubbles

Under low ionospheric activity, EDPs tend to resemble a slow function (Culverwell and Healy, 2015). Under high activity periods and during the transition between day and night time, there is a higher incidence of regions of localized irregularities, plasma bubbles, which lead to a sharper gradient in electron density (Jiao and Morton, 2015; Kepkar et al., 2020). Such regions are responsible for large, medium, and small-scale irregularities (Xiong et al., 2016), which specifically corresponds to sizes up to the Fresnel scale. In a RO geometry and especially in the range of ionospheric altitudes where the bending is significantly smaller than in neutral atmosphere (Kursinski et al., 1997), the Fresnel scale is given by

$$d_F = 2\sqrt{\frac{\lambda L_t L_r}{L_t + L_r}}, \quad (9)$$

$$d_F \approx 1.5 \text{ km}, \quad (10)$$

125 where λ is L1 band wavelength, L_t is the horizontal distance of the GPS satellite to the Earth's limb ($\sim 28.5 \times 10^6$ m), L_r is the LEO horizontal distance ($\sim 3.4 \times 10^6$ m, assuming an altitude orbit of 820 km). The propagation through these irregularities results in diffraction and refraction of the electromagnetic field. The occurrence of these effects are observed as abrupt fluctuations in amplitude and phase, referred to as scintillations (Aarons, 1982; Yeh and Liu, 1982; Wickert et al., 2004; Zeng and Sokolovskiy, 2010). Moreover, the presence of plasma bubbles introduces asymmetries between the inbound (GPS to tangent point) and outbound ray trajectories (tangent point to LEO). This condition contradicts the assumption of spherical symmetry of the atmosphere in retrievals via Abel transform (Fjeldbo et al., 1971) and it is related to high-order terms composing the bias after the standard ionospheric correction (Vorob'ev and Krasil'nikova, 1994). The high-order bias, critical in meteorological and climate applications, are handled either by Kappa or Bi-local correction (Healy and Culverwell, 2015; Liu et al., 2020).



3.1.1 Single bubble

The location estimation of the plasma bubbles in F-region is a complicated task in RO measurements. The ray path between
 135 GPS and LEO satellites includes ionospheric propagation in two segments, i.e., ray inbound and outbound. The disturbance
 observed in the sampled signal and originated during either the first or the second segments cannot be visually distinguished.
 The back propagation (BP) method has been used to detect irregularities in F-region in studies using both simulations and real
 occultation measurements (Sokolovskiy et al., 2002; Cherniak et al., 2019).

However, there is a lack of RO events combined to collocated data provided by different systems where the true location of
 140 the irregularity region is precisely known. In our study, the model of isotropic irregularities representing a plasma bubble in
 the equatorial region is considered in WOP simulations to evaluate the estimation obtained with BP method. The model has
 been described in Carrano et al. (2011) and corresponds to an occultation performed by C/NOFS satellite and collocated with
 an incoherent scatter radar and a ground-based receiver in VHF band. The collocated data allowed to have a good estimation
 of the placement and size of the bubble, besides the parameters required in the modelling of the disturbance observed in the
 145 occultation measurement.

The plasma bubble is modelled by a 2-D random realization of Gaussian variables filtered by the spectral density function
 (SDF),

$$\Phi_{\Delta\rho}(k_x, k_y) = 4\pi k_0^{(2\nu-2)} \frac{\Gamma(\nu)}{\Gamma(\nu-1)} \frac{1}{(k_0^2 + k_x^2 + k_y^2)^\nu}, \quad (11)$$

where $k_{x,y}$ are the wave numbers in the propagation and vertical direction, $k_0 = 2\pi/L_0$ is the outer scale wave number, Γ is
 150 the Euler's gamma function and ν denotes the spectral slope. The filtered variables,

$$\Delta\rho(x, y) = \mathfrak{F}^{-1} \left\{ \sqrt{\Phi_{\Delta\rho}(x, y)} SF r_m \right\}, \quad (12)$$

are modulated to the electron density model,

$$\rho = \rho_b [1 + \Delta\rho \times \sigma_{\Delta\rho/\rho} \times B], \quad (13)$$

where ρ_b is the background EDP, B is a envelope function defining the x -position of the plasma bubble and $\sigma_{\Delta\rho/\rho}$ is the RMS
 155 level of the fluctuations. In (12), r_m corresponds to the grid of Gaussian random numbers and $SF = L/2\pi$ is a spatial factor
 in which L is the bubble vertical extension. The bubble width is controlled with the Gaussian envelope function,

$$B(x, y) = e^{-\frac{[\alpha(x,y) - \alpha_0]^2}{2\sigma_\alpha^2}}, \quad (14)$$

in which the function maximum and the bell width are set as

$$\alpha_0 = \tan^{-1} \left(\frac{x_0}{hmF2 + R_e} \right), \quad (15)$$

$$160 \quad \sigma_\alpha = \frac{L_H}{A(hmF2 + R_e)}, \quad (16)$$



where x_0 denotes the bubble placement in x -direction, $hmF2$ is the F-region electron density peak height, L_H corresponds to the bubble width, R_e is the Earth's radius and the scaling factor $A \approx 1.348$. The set of parameters estimated in Carrano et al. (2011) were used in our WOP simulation to replicate the scintillation in the total field with equivalent deterministic properties. Figure 4 shows the Gaussian envelope and the filtered random realization modulated to the electron density model.

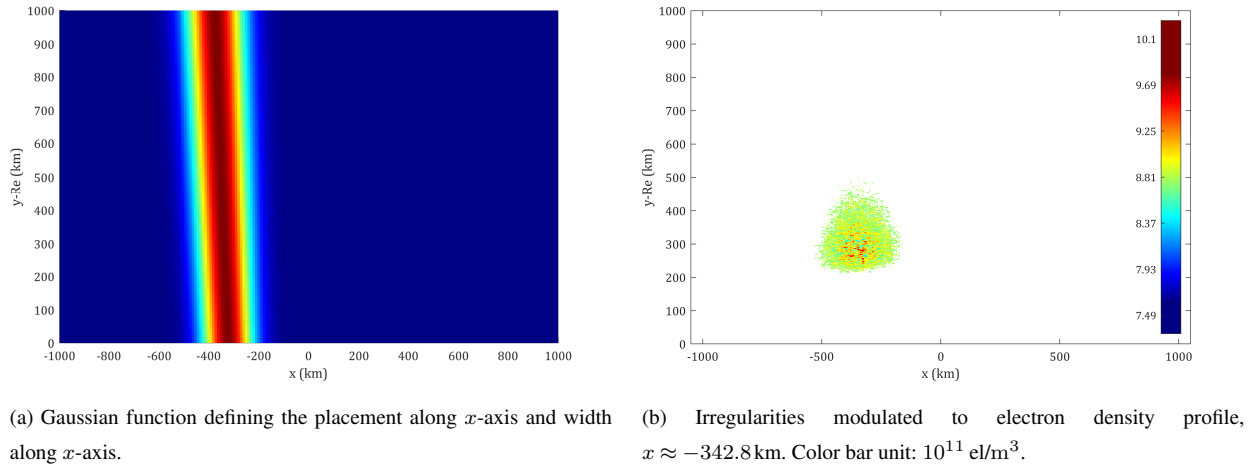


Figure 4. Bubble modelling.

165 Figure 5 shows the normalized signal intensity at the observational plane and the power spectral density (PSD) computed within 280 km and 340 km. The results have good agreement with the ones reported in Carrano et al. (2011) and validate our WOP simulation.

Then, the simulated total field disturbed by the plasma bubble during the propagation is considered as the boundary condition to the BP method. The scenario is used as the base model of different test cases for capabilities and limitation assessment of
 170 the BP method in the presence of a single plasma bubble, namely:

- Accuracy of the location estimate along x -axis: the position of the region of irregularities is controlled by modifying x_0 in (14);
- Accuracy of the location estimate along x -axis with different RMS fluctuation levels: the level of irregularities modulated to the EDP is defined by $\sigma_{\Delta\rho/\rho}$ in (13);
- 175 – Accuracy of the location estimate along x -axis with different vertical extensions of the bubble;
- Accuracy of the location estimate along x -axis with different bubble width: the extension along x -axis is controlled by L_H in (16.)

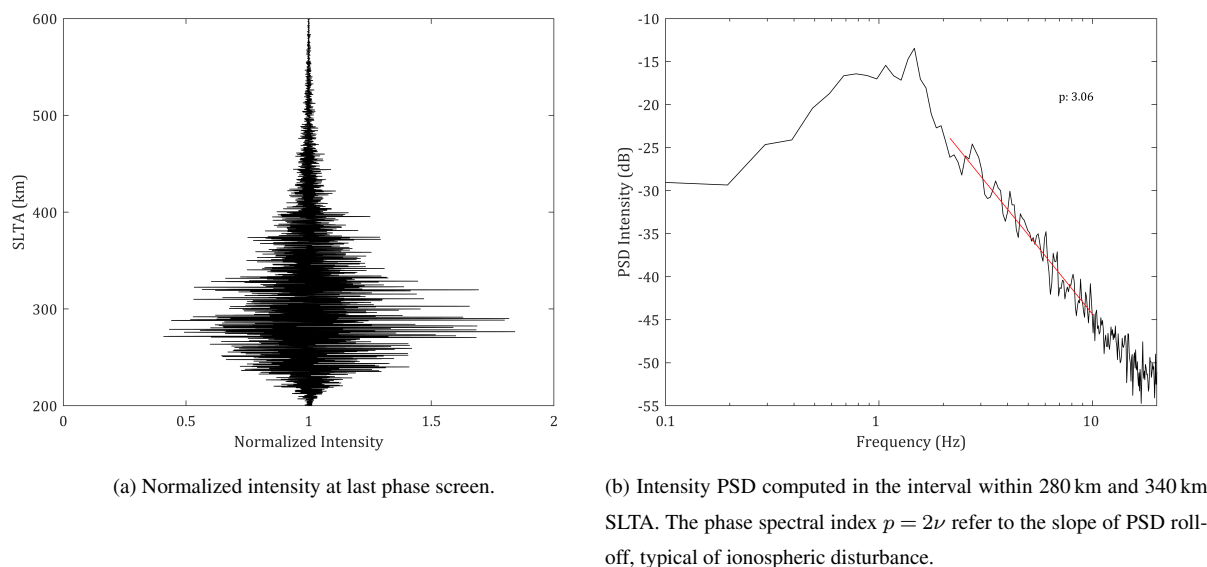


Figure 5. WOP simulation results assuming set of parameters described in Carrano et al. (2011). The original C/NOFS measurement had average SNR level around 1500 V/V.

3.1.2 Multiple bubbles

In addition to the single bubble cases, a second plasma bubble was added to the ray trajectory by superposing another envelope function to the one shown in Fig. 4(a), simply assuming a different x_0 in (14). The test cases with two plasma bubbles allow us to evaluate the BP method under the following scenarios:

- Accuracy of the location estimate along x -axis for the two plasma bubbles;
- Accuracy of the location estimate to different separation distances between bubbles;
- Accuracy of the location estimate when bubbles have different RMS fluctuation levels.

4 Results

In the simulations, the filtered random field was modulated with an EDP modelled by the Chapman's function (Culverwell and Healy, 2015) considering the F-region peak ($nmF2 = 8.81 \times 10^{11} \text{ el/m}^3$), height ($hmF2 = 288.5 \text{ km}$) and scale height ($H = 31 \text{ km}$) according to the EDP described in Carrano et al. (2011).

The WOP simulations of the test cases did not include the propagation to LEO orbit via the diffraction integral (1). Therefore, Zverev transform (5,6) is applied since the resultant field is given on the vertical plane. The WOP signals shown in figures include instrument noise, which assumed a MetOp-A (Meteorological Operational satellite) occultation in low latitude as



reference to the SNR level (see Appendix A). This occultation extends up to 600 km SLTA, an exceptional feature compared to nominal MetOp occultations. Normally, the GNSS signal is tracked up to around 100 km SLTA but an experimental campaign during MetOp-A end-of-life operation had its SLTA range extended to the point where the F-region is included. Different than
 195 in the neutral atmosphere region, the SNR level decays with altitude due to the antenna pattern. At this particular measurement (and in simulations), the SNR reference level assumed to estimate the instrumental noise strength at F-region peak is around 600 V/V.

The BP planes were computed at every 10 km, which defines the precision of the estimations in our implementation. The BP amplitudes were detrended with 3-pass Savitzky-Golay of 2nd order (Zeng et al., 2019), assuming a 10-km window length
 200 following the outer scale. The figures show the BP amplitudes at every 50 km (black line) and the root-mean square value of the detrended amplitudes, i.e., standard deviation (σ_u), computed on every plane (blue line). Its global minimum estimates the position of the plasma bubbles along the ray path (x -axis).

4.1 Single bubble

Fig. 6 shows the BP amplitudes when bubbles were placed at $x = -342.8$ km and assumed RMS fluctuation level $\sigma_{\Delta\rho/\rho} = 17\%$
 205 (Carrano et al., 2011). The contour lines depict the plasma bubbles in the background of the BP amplitudes.

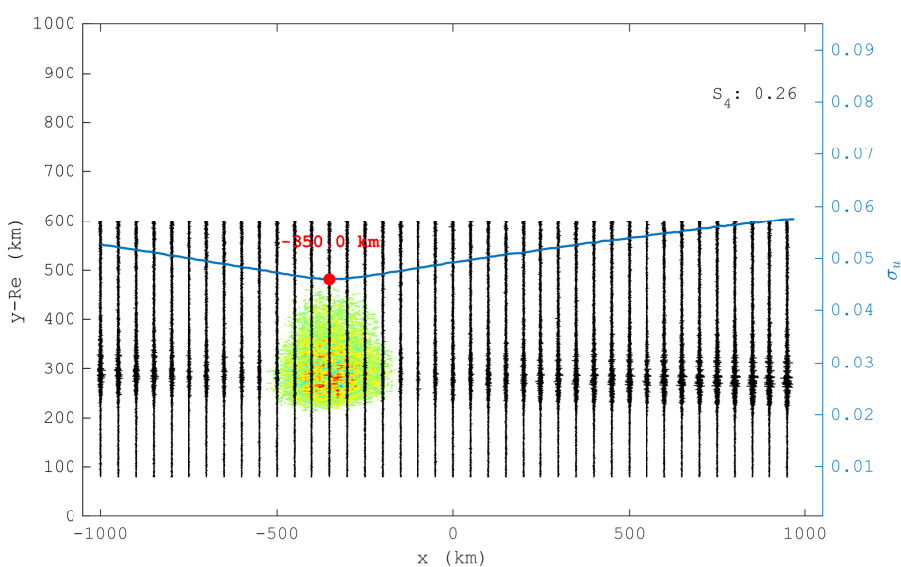


Figure 6. Single bubble at $x = -342.8$ km, $\sigma_{\Delta\rho/\rho} = 17\%$. Estimation error $\varepsilon_x = -7$ km.

The RMS fluctuation level corresponds to a variation in electron³ density between $\sigma_{\Delta\rho/\rho} \approx \pm 1.5 \times 10^{11}$ el/m³, which results in weak scatter ($S_4 = 0.26$) in agreement to Carrano et al. (2011). The estimate error corresponds, i.e., $\varepsilon_x = x_0 - x_{\min}(\sigma_u) = -7$ km. Fig. 7 shows the result considering the bubble placement on the left side of the box (ray path outbound).

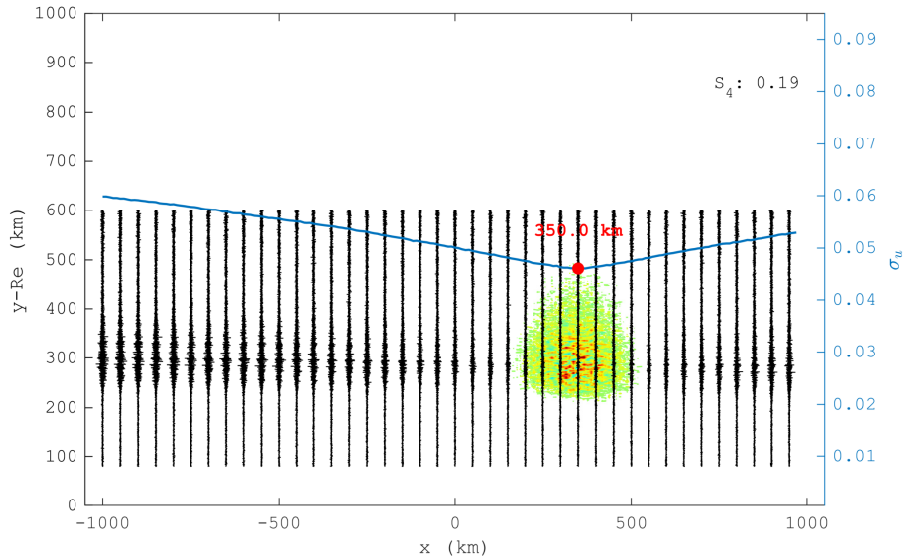


Figure 7. Single bubble at $x = 342.8$ km, $\sigma_{\Delta\rho/\rho} = 17\%$. Estimation error $\varepsilon_x = -7$ km.

In the single bubble scenario, the location estimate has good accuracy regardless of the placement in the inbound (left) or
 210 outbound sector (right). Therefore, the location estimate in a single bubble scenario is limited by the precision considered in
 the BP method, herein 10 km. The minor difference in scintillation index is related to the filtered random variables assumed in
 the bubble model, which can create an variation in the resultant electron density assumed in the simulation.

4.1.1 Influence of RMS fluctuation level

A parametric evaluation of $\sigma_{\Delta\rho/\rho}$ was performed to assess the minimum fluctuation level in which the bubble is detectable
 215 with BP method. Figure 8 shows the box chart comparing the sensitivity of the detection in three different levels, $\sigma_{\Delta\rho/\rho} =$
 2.5% , 3.0% and 17% (reference case) in term of estimation accuracy along x-axis, and the correspondent standard deviation
 curves.

The curve corresponding to $\sigma_{\Delta\rho/\rho} \leq 2.5\%$ (red curve) does not have a convex shape, i.e, a clear global minimum. The
 location estimate is determined by the noise level, since its overall level lies beneath the threshold value, $\sigma_u \approx 0.0456$ within
 220 F-region, see Fig. 8(b) and Fig. A(b). Thus, this indicates that the estimations are not reliable as long as $\sigma_u \leq \sigma_0$. For RMS
 fluctuation levels $\sigma_{\Delta\rho/\rho} \geq 3.0\%$ ($\pm 2.64 \times 10^{10}$ el/m³), the region of irregularities are detectable with median $x = -370$ km and
 the interval $[-435, -280]$ km corresponding to 50% of estimates, $-63 < \varepsilon_x < 90$ km. Regardless, $\sigma_{\Delta\rho/\rho} = 3.0\%$ represents
 $S_4 < 0.1$, far below the low scintillation threshold ($S_4 = 0.2$). An accuracy around the method precision (10 km) for 50% of
 the realizations was achieved for the reference case ($\sigma_{\Delta\rho/\rho} = 17\%$).

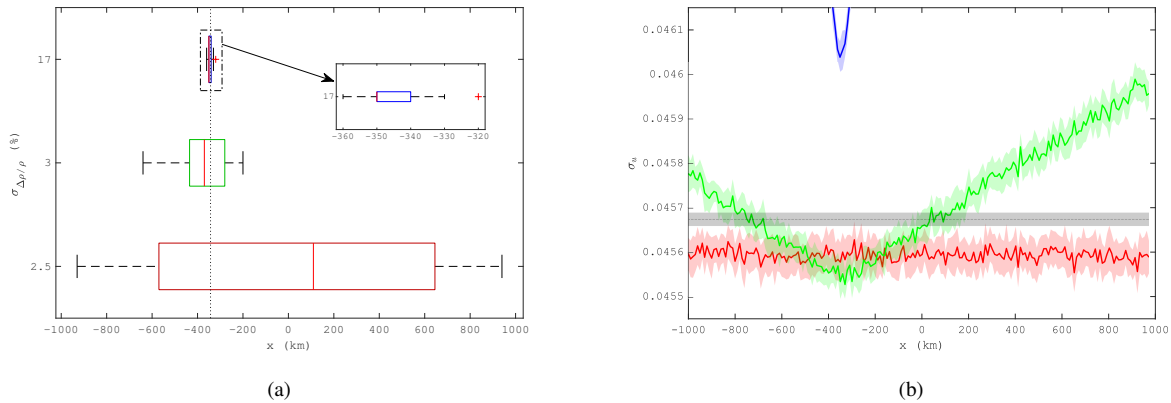


Figure 8. Influence of fluctuation level assuming a single irregularity region in simulation. (a) Box chart comparing different RMS fluctuation levels. Vertical dashed line indicates the placement of the bubble. The detection improves significantly when the fluctuation correspond to $\sigma_{\Delta\rho/\rho} \geq 3.0\%$ ($\pm 2.64 \times 10^{10}$ el/m³), with estimate median $\bar{x} = -370$ km. Weaker irregularities, such as $\sigma_{\Delta\rho/\rho} = 2.5\%$, are not distinguishable from the receiver noise and yields poor location estimate of the irregularity patch. (b) Standard deviation of BP amplitudes. Shade regions stands for 1 σ -interval. Same color scheme in both figures. Data corresponds to 20 realizations for each fluctuation level.

225 4.1.2 Influence of bubble vertical extension

Figure 9 shows the comparison between the location estimate obtained with WOP amplitudes assuming different vertical thickness of the irregularity region and $\sigma_{\Delta\rho/\rho} = 17\%$. The extension was controlled by applying a Tukey window to the right term in (13).

The black dashed curve shows the standard deviation curve for the bubble with original dimensions, in which the effective
 230 extension of the bubbles is defined by the region around the F-region with electron density within 75% of the peak value (~ 60 km) (Carrano et al., 2011). The maximum estimation error observed in simulations was -17.2 km when the bubble extended vertically along 30 km. This result implies the higher variability in the estimation as the global minimum approaches the noise level, i.e., $\sigma_u \approx \sigma_0$. In the thinnest layer, the estimation error was 13 km.

Nevertheless, the results indicate that the estimation is acceptable even for the thinnest layer. Despite the peak assumed
 235 in the simulation being located in F-region, the vertical extensions shorter than 2.5 km resemble the thickness of an sporadic E-layer (Zeng and Sokolovskiy, 2010; Arras and Wickert, 2018). This result confirms the capability presented in (Gorbunov et al., 2002; Cherniak et al., 2019), apart from a potential advantage in accuracy due to the higher SNR level (lower noise floor) around 100 km (see Fig. A(b)). The analysis of sensitivity level and estimation accuracy of sporadic E-layers are beyond the scope of this study.

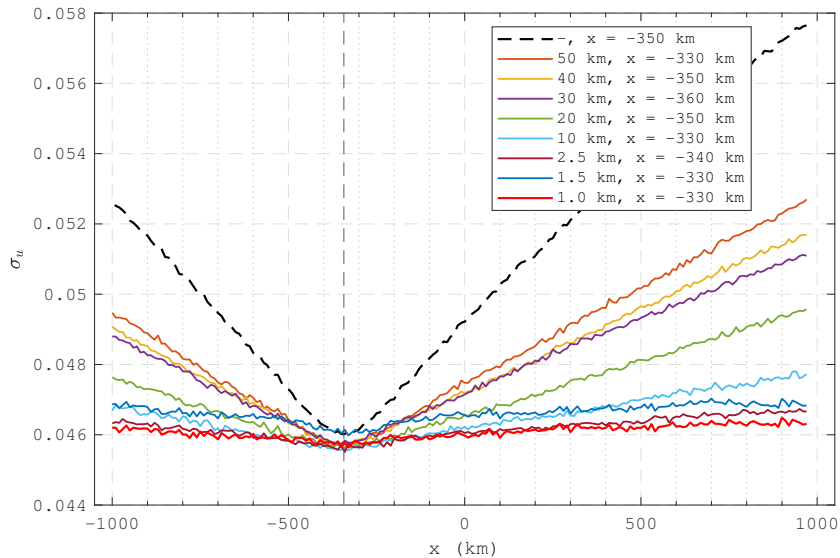


Figure 9. Standard deviation curves in scenarios assuming different vertical extensions of a single bubble in inbound region and $\sigma_{\Delta\rho/\rho} = 17\%$. Black dashed corresponds to the original case. Location estimate is possible up to thinnest layer, resembling sporadic E-layer dimension. Maximum estimation error $\sigma_x = -17$ km. Vertical dashed lines indicates the placement of the irregularity patch.

240 4.1.3 Influence of bubble width

Figure 10 shows results for scenarios assuming different bubble width and fixed fluctuation level ($\sigma_{\Delta\rho/\rho} = 17\%$). A region with extension $L_H \leq 20$ km creates low scintillation in the GNSS signal ($S_4 < 0.2$) but it is still detectable and with estimation error $\varepsilon_x = 10$ km. Narrower regions do not show a clear global minimum, since the disturbances are at the same level as the receiver noise.

245 The detection of irregularities is theoretically possible even for $L_H > 600$ km, which leads to higher disturbances as shown by the scintillation index. However, the uncertainty about its center estimate increases proportionally to the region width, despite the increasing difference between global minimum level and the noise floor. Thus, the extension of the irregularity region must be shorter than the distance between GNSS and LEO satellites, as stated in (Sokolovskiy et al., 2002).

4.2 Multiple bubbles

250 Fig. 11 shows two bubbles symmetrically placed around the origin, $x_1 = -342.8$ km (left) and $x_2 = 342.8$ km (right), and with the same fluctuation level ($\sigma_{\Delta\rho/\rho} = 17\%$). The global minimum σ_u corresponds to the bubble placed on the right side, the last irregularity region along the ray path (forward propagation). The accuracy of the location estimate is affected significantly by the presence of the second bubble and by the instrument noise, yielding an estimation error $\varepsilon_x \approx -123$ km. The location estimate of the left bubble is a rather complicated task since the presence of the predominant patch (left side) shadows its

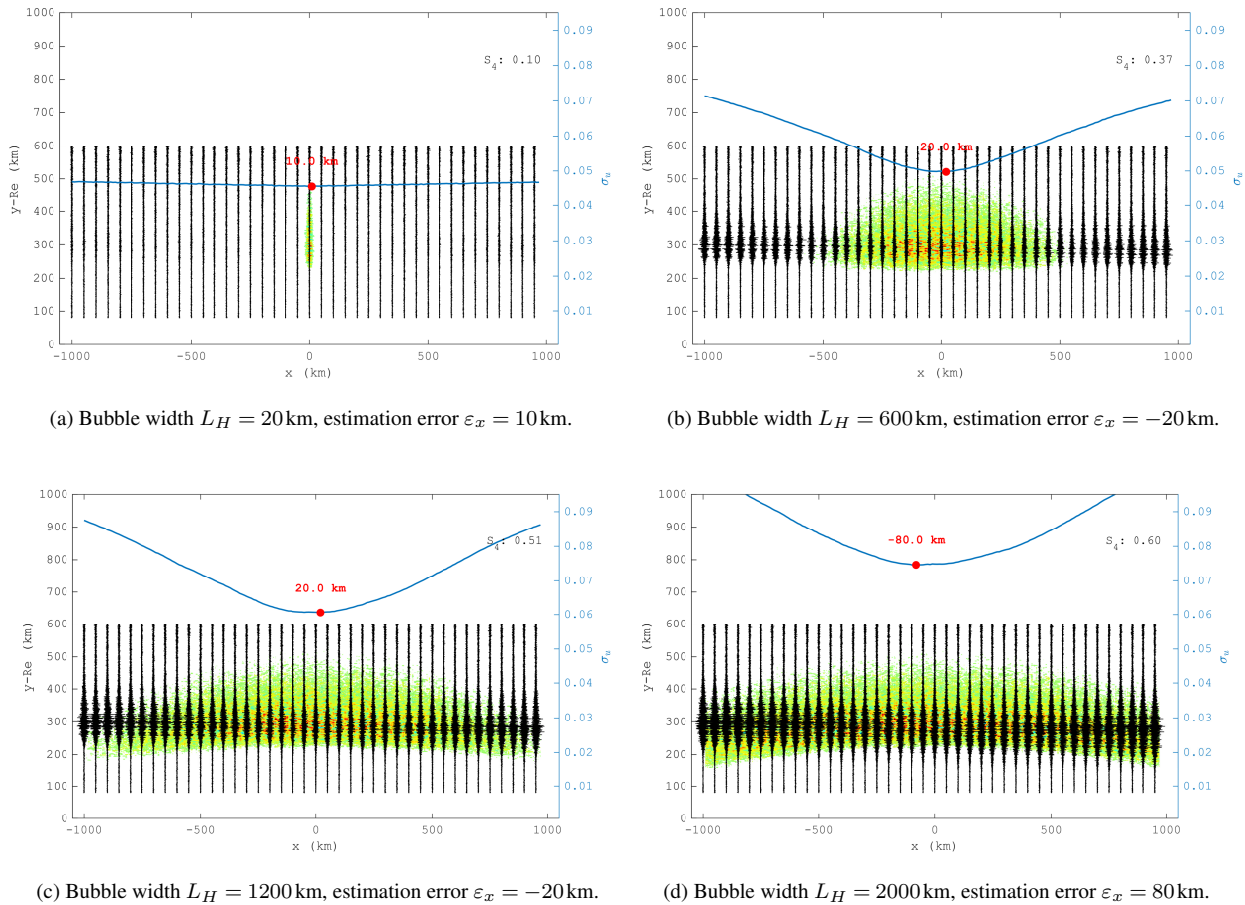


Figure 10. Single bubble with different widths (L_H). The detection is possible when $L_H > 20$ km but estimate accuracy (patch center) decreases with increasing width.

255 contribution to the total wave field and, therefore, a clear local minima is not detectable in the standard deviation of the BP amplitudes.

Fig. 12 shows the scenario with a larger separation between the irregularity regions, $\Delta x = 1200$ km. The minima become more distinguishable with the larger distance between the two regions, and this aspect slightly improves their location estimates. The most accurate estimation is given nevertheless on the right bubble ($\varepsilon_x \approx -80$ km), with the instrument noise having a
 260 partial contribution in the error. Regarding the left bubble, there is a clearer indication of the irregularity placement in the inbound sector, around $x = -500$ km, but with the estimation error greater than for the predominant patch.

A comparison between Figs. 10(c,d) (wide bubble scenarios) and Figs. 11 and 12 shows that it is possible to distinguish cases with a single wide irregularity region from a scenario with multiple smaller bubbles, since the latter would likely present more than one local minima along the ray path. Even though, the location estimate of the secondary patch is less reliable.

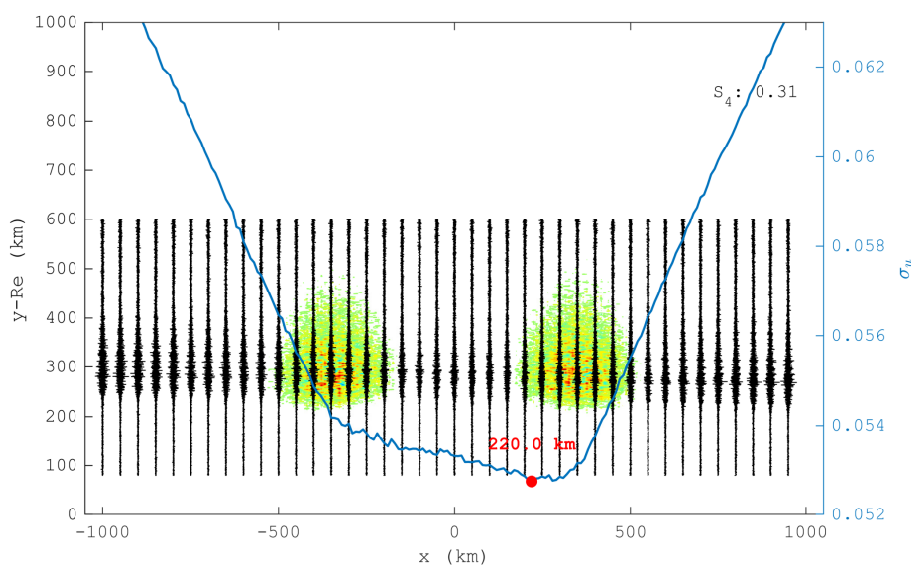


Figure 11. Bubbles at $x_1 = -342.8$ km and $x_2 = 342.8$ km, $\sigma_{\Delta\rho/\rho} = 17\%$. Estimation error $\varepsilon_{x_2} = -123$ km.

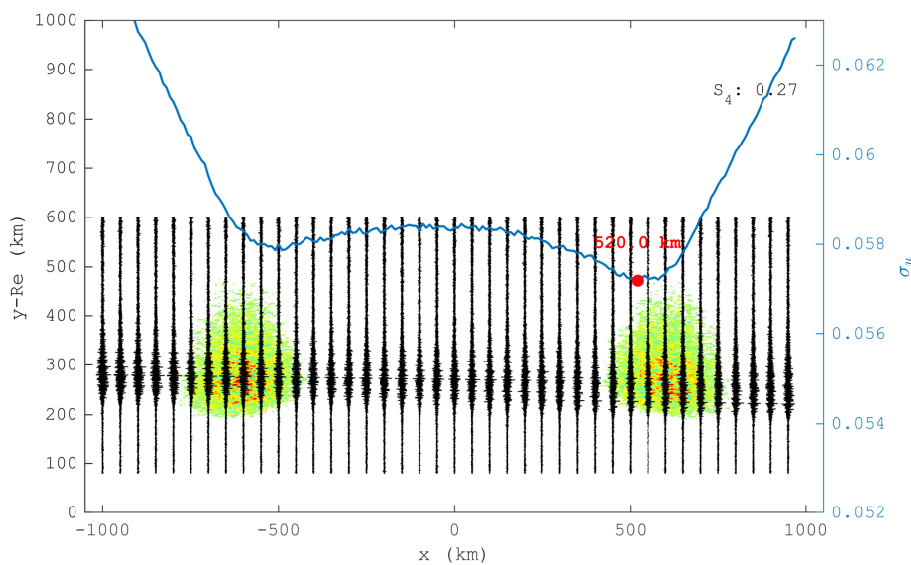


Figure 12. Bubbles at $x_1 = -600$ km and $x_2 = 600$ km, $\sigma_{\Delta\rho/\rho} = 17\%$. Estimation error $\varepsilon_{x_2} = -80$ km and a clearer indication of the secondary bubble's placement along the ray path.



265 In contrast to single region cases where the predominant constraint to detection is the noise level ($\sigma_u \approx \sigma_0$), the results indicate that the separation between the regions has major influence in the detection/location task of multiple patches.

4.2.1 Influence of RMS fluctuation level

The RMS fluctuation level of one of the bubbles was kept constant ($\sigma_{\Delta\rho/\rho} = 17\%$) while the other had the fluctuation set to weaker values. Fig. 13 depicts the results assuming $\sigma_{\Delta\rho/\rho} = 6\%$ and $\sigma_{\Delta\rho/\rho} = 12\%$.

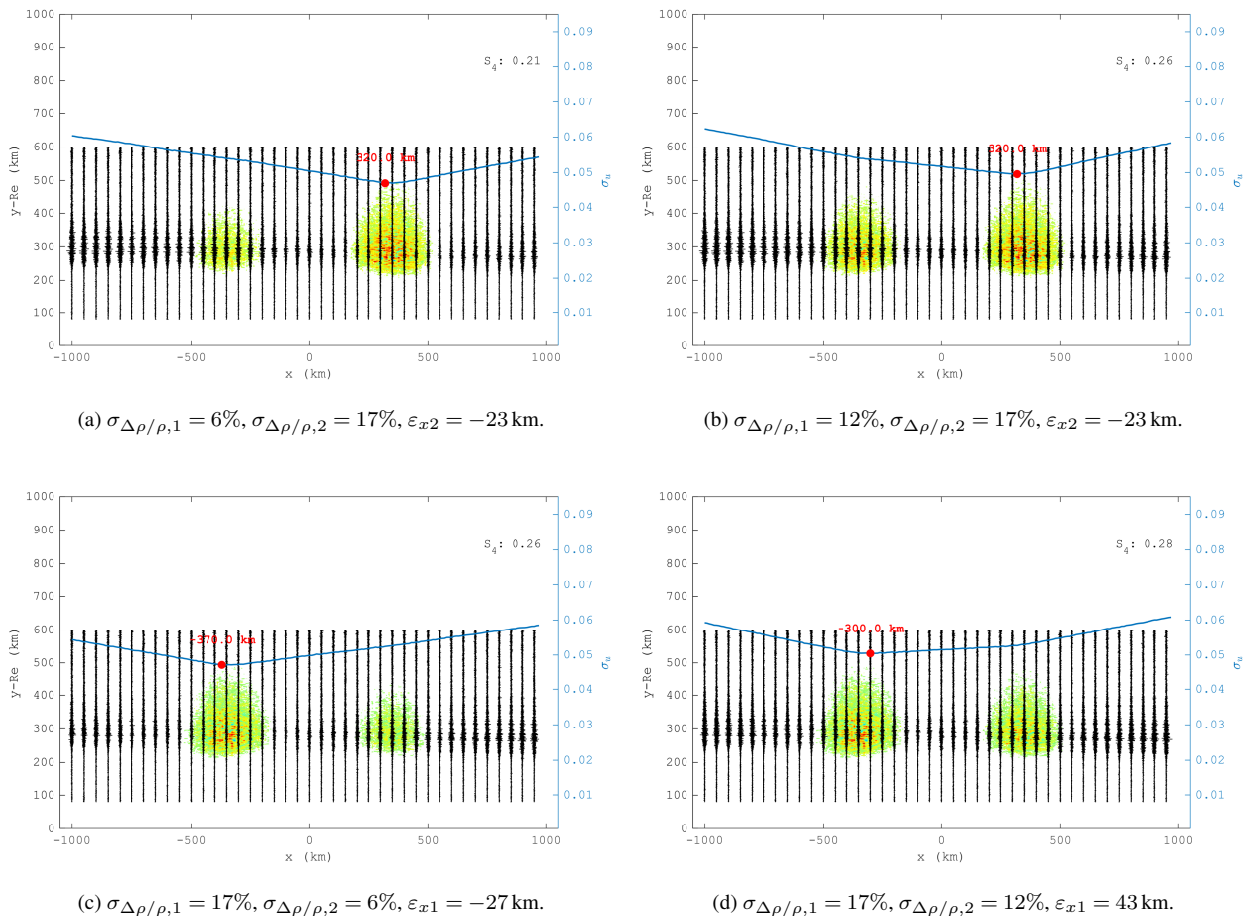


Figure 13. Bubbles at $x = \pm 342.8$ km with weaker RMS fluctuation level on the left (a,b) and the right bubble (c,d).

270 The standard deviation curves in scenarios including a bubble with $\sigma_{\Delta\rho/\rho} = 6\%$ are similar to the one observed in the scenario of a single bubble (see Fig. 6 and 7). However, the location of the global minima along x -axis differs, indicating that the presence of a second bubble affects the location estimate of the predominant irregularity region. The remarks are valid despite the placement of the weaker region at the inbound or outbound sector.



Figure 14 shows the comparison of standard deviation curves assuming different RMS fluctuation levels on the bubble placed
 275 at the inbound sector.

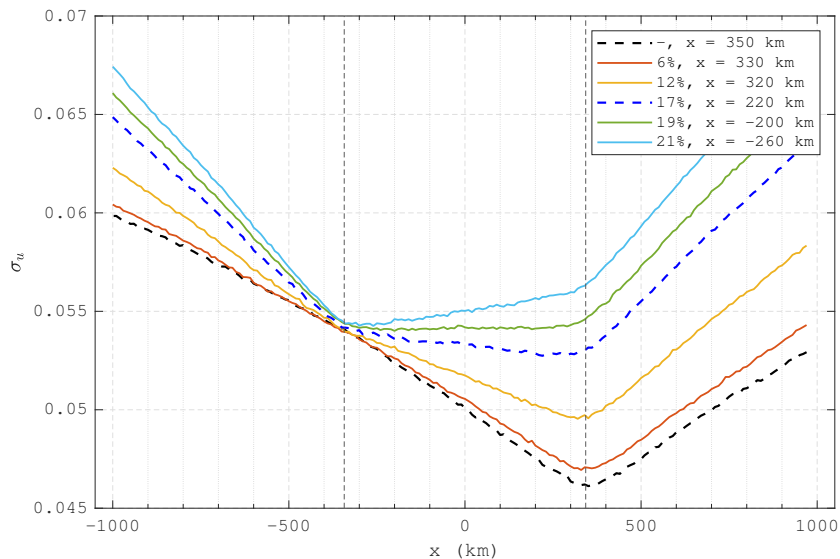


Figure 14. Comparison between simulations assuming different RMS fluctuation levels on the left bubble and constant on right bubble ($\sigma_{\Delta\rho/\rho,2} = 17\%$). The legend shows $\sigma_{\Delta\rho/\rho,1}$ and the location estimate of the right bubble along x , after σ_u global minimum. Vertical dashed lines depict the placement of the irregularity regions in the simulations (± 342.8 km). Black dashed line relates to the case of a single bubble at the outbound sector. Blue dashed lines correspond to the scenario shown in Fig. 11.

A clear shift of the global minimum towards the weaker patch is observed around $x = 342.8$ km as $\sigma_{\Delta\rho/\rho,1}$ increases from 6% to 17% ($\sigma_{\Delta\rho/\rho,1} = \sigma_{\Delta\rho/\rho,2}$), which leads to a gradual increase in the estimation error. Nonetheless, higher RMS fluctuation levels also make the left bubble more detectable. After $\sigma_{\Delta\rho/\rho,1} > \sigma_{\Delta\rho/\rho,2}$, the left bubble becomes dominant, and therefore the estimation is related to the bubble at the inbound region.

280 4.3 Analysis COSMIC occultations results

The remarks made after simulations are used in the evaluation of two COSMIC occultations presented in Cherniak et al. (2019). The measurements were performed during a severe geomagnetic storm between June 22nd – 23rd, 2015. Their results are replicated in Fig. 15 after using (4) to compute the BP amplitude at $x = 3000$ km, followed by employing (5,6) recursively to obtain the total field at the other auxiliary planes.

285 The global minima are found between 2600 – 2800 km in both occultations, indicating the position of the main region of irregularities along the ray path. In Fig. 15(b), the height range around 100 km has not been included in the calculation of the BP amplitude standard deviation. The disturbances are certainly due to the presence of sporadic E-layer (Arras and Wickert,

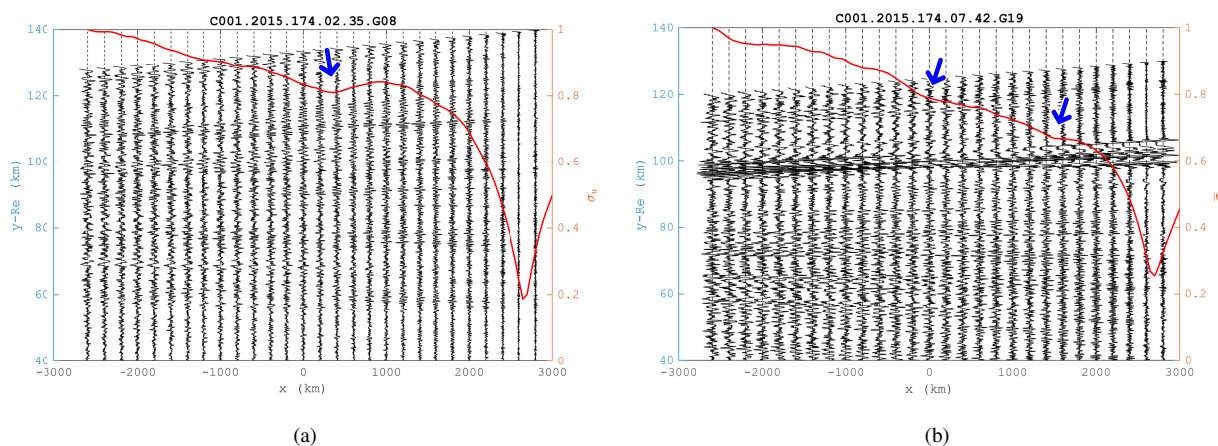


Figure 15. BP amplitudes of COSMIC occultations during geomagnetic storms. Right y -axis corresponds to the values of the normalized BP amplitude standard deviation (red curve). The global minimum in the red curves estimate a similar position of the main irregularity region for both occultations ($x = 2600 - 2800$ km). The arrows highlight local minima, which may indicate the existence of other regions of ionospheric irregularities. Measurement average SNR level (a) 564 V/V, (b) 694 V/V.

2018; Zeng and Sokolovskiy, 2010) and not to irregularities in the F-layer. The computation of the standard deviation within the height range provides its location estimate (Gorbunov et al., 2002; Cherniak et al., 2019).

290 As seen in simulations, the existence of other local minima in the standard deviation curve gives the indication of not only one but two or more irregularity regions during the occultations. The arrows point out the approximate location of these local minima in Fig. 15. The confirmation about the existence of such regions requires collocated measurements, similar to the case reported in Carrano et al. (2011). In addition, the existence of multiple regions has shown to reduce to some extent the location estimate accuracy given by the global minimum. In reality, the main irregularity region could have been placed
 295 slightly farther away from the LEO satellite than as indicated by the BP method estimation.

5 Conclusions

The capability of back propagation to detect irregularity regions in F-layer, e.g., ionospheric plasma bubbles, has been assessed with WOP simulations. The reference case corresponded to a single bubble at the inbound sector observed in a C/NOFS occultation, in which the location, size, and distance from LEO orbit have been confirmed with collocated data (Carrano et al.,
 300 2011). The same model of isotropic irregularities was applied to all the other test scenarios evaluated with WOP simulations.

In the simulation of single bubble scenarios, the location estimate accuracy of the irregularity region along the ray path was ~ 10 km for the reference case ($\sigma_{\Delta\rho/\rho} = 17\%$). The bubble placement in either inbound or outbound region did not affect the detection and location estimate of the irregularity regions. Additionally, the detection of bubbles has been possible regardless of the region width. However, the accuracy of the center estimate decreases with increasing width.



305 In multiple bubble scenarios, the ability to resolve bubbles requires the patches to be well separated. Then, the regions are
detectable but the accuracy of the estimate differs. The region yielding the stronger disturbance (predominant) has the most
accurate location estimate. However, a bias towards the secondary bubbles is inherent and it increases with the RMS fluctuation
level. If secondary bubbles have a very weak fluctuation, the patch is shadowed by the dominant region and their existence can
be untraceable. In the case of bubbles with similar intensities and aligned, the most accurate estimation has been given in the
310 latest region along the forward propagation direction.

Most importantly, the capability of detection/location of irregularity patches has shown to be limited by the receiver noise
level, i.e., localizing irregularity patches with the BP method is unfeasible when the noise amplitude is stronger than the am-
plitude of the ionospheric scintillation ($\sigma_u < \sigma_0$). At the SNR level assumed as the reference in our simulations (MetOp), even
irregularity patches in F-region corresponding to low scintillation, corresponding to $\sim \pm 2.64 \times 10^{10} \text{ el/m}^3$, were detectable.
315 This fluctuation corresponds to the local gradient within the bubble region and, therefore, also depends on the local mean
density (background EDP), patch size, and distance between the bubble and receiver.

The SNR level as well as the highest SLTA point in occultations differs in different RO missions. A SLTA range which
includes the ionospheric layer, i.e., further than around 100 km SLTA as seen in the experimental MetOp-A campaign, is an
important feature to accurately detect and locate the ionospheric plasma bubbles in RO measurements. A minimized influence
320 of the antenna gain in higher SLTA might also contribute to improve the results obtained with BP method. Nonetheless, our
results indicate that the present operating SNR level in MetOp constellation is sufficient to detect even low scintillation levels.

The information about the irregularities regions location, e.g., plasma bubbles, is relevant in irregularity modelling and po-
tentially could support the mapping of such phenomena and its climatology. Our results should be taken as complementary to
the investigations described in Gorbunov et al. (2002); Sokolovskiy et al. (2002); Cherniak et al. (2019). Further evaluations
325 of occultations collocated with data provided by different techniques, on the lines of Carrano et al. (2011), are required to
thoroughly evaluate the method capabilities, also regarding E-layers. In combination with the location along x , the horizontal
and vertical extension of the plasma irregularity are also parameters of great interest to model the plasma irregularities. Ap-
proaches that could estimate such features, as well as the location of secondary regions (not given by global minimum), should
be investigated in future works.

330 Appendix A: Including instrument noise in WOP signals

In WOP simulations, the signal transmitted by the GNSS (boundary condition) is assumed to be a cylindrical wave. The
propagation between GNSS satellite and the first phase screen occurs in free space, with amplitude decay $\propto 1/\sqrt{r}$. For the
sake of practicality, the complex signal is normalized on the first PS. Then, the medium refractivity is recursively accounted
by modifying the instant phase of the incident wave and propagating it in vacuum until the next neighbouring phase screen
335 (Knepp, 1983). At the last PS, the normalized complex signal in the WOP (\hat{u}) can model a real signal by using a constant
calibration factor, A , viz

$$u_{\text{signal}}(t) = A\hat{u}(t). \quad (\text{A1})$$



The total signal will also include noise,

$$u_{total}(t) = u_{signal}(t) + u_{noise}(t). \quad (A2)$$

340 We use the measured SNR from a real occultation signal to find the appropriate noise level to be added in the WOP amplitude,

$$\hat{u}_{noise}(t) = \frac{1}{A} u_{noise}(t), \quad (A3)$$

$$\hat{u}_{total}(t) = \hat{u}(t) + \hat{u}_{noise}(t). \quad (A4)$$

The noise in occultation measurements has several sources: thermal noise in the receiver; clock noise; co-channel noise. For this task, we assumed a normal distribution to model the white noise, i.e., $X, Y \sim \mathcal{N}(\mu, \sigma^2)$, where μ is the mean value and σ^2 is the variance. Then, the noise in the i -th sample is

$$u_{noise}(t_i) = \sigma_0(X + jY)/\sqrt{2}, \quad (A5)$$

$$\sigma'_0 = \sigma_0/A, \quad (A6)$$

$$\hat{u}_{noise}(t_i) = \sigma'_0(X + jY)/\sqrt{2}, \quad (A7)$$

where $X, Y \sim \mathcal{N}(0, 1)$. Next, we obtain the average noise power (approximation due to the finite number of samples) by multiplying the noise with its complex conjugate and taking the average over a large time window,

$$P_{noise} = \langle u_{noise} u_{noise}^* \rangle \approx \sigma_0^2. \quad (A8)$$

Likewise, the averaged signal power becomes

$$P_{signal} = \langle u_{signal} u_{signal}^* \rangle \approx A^2 \langle \hat{u} \hat{u}^* \rangle. \quad (A9)$$

The SNR in terms of the signal and noise power, with units [W/W], is given by

$$355 \quad SNR_W = \frac{P_{signal}}{P_{noise}} \approx \frac{A^2 \langle \hat{u} \hat{u}^* \rangle}{\sigma_0^2}. \quad (A10)$$

Hence,

$$\sigma_0 = \sqrt{\frac{A^2 \langle \hat{u} \hat{u}^* \rangle}{SNR_W}}, \quad (A11)$$

and

$$\sigma'_0 = \sqrt{\frac{\langle \hat{u} \hat{u}^* \rangle}{SNR_W}}. \quad (A12)$$

360 In case different sample rates are used in the measurements and the simulations, one has to take into account the sample rate or the bandwidth (B), where

$$B \propto f_s, \quad (A13)$$



in which f_s is the sample rate in Hz. The noise power is given by

$$P_{noise} = BN_0, \quad (A14)$$

365 where N_0 is the noise power density in W/Hz, which is assumed to be a distinct constant for each occultation. Thus, the SNR to be assumed in the simulations is related to the measured SNR as

$$SNR_{W,WOP} = \frac{P_{signal}}{P_{noise,WOP}} = \frac{P_{signal}}{P_{noise}} \frac{B}{B_{WOP}} = SNR_W \frac{B}{B_{WOP}} = SNR_W \frac{f_s}{f_{s,WOP}}. \quad (A15)$$

Then, the final formula for the noise amplitude to be added to the WOP signal is

$$\sigma'_0 \approx \sqrt{\frac{\langle \hat{u} \hat{u}^* \rangle}{SNR_{W,WOP}}} = \sqrt{\frac{\langle \hat{u} \hat{u}^* \rangle}{SNR_W} \frac{B_{WOP}}{B}} = \sqrt{\frac{\langle \hat{u} \hat{u}^* \rangle}{SNR_W} \frac{f_{s,WOP}}{f_s}}. \quad (A16)$$

370 Conventionally, the SNR is described in terms of voltage ratio in the RO community. In this way,

$$SNR_W [W/W] = SNR_V^2 [V/V]. \quad (A17)$$

Finally,

$$\sigma'_0 \approx \sqrt{\frac{\langle \hat{u} \hat{u}^* \rangle}{SNR_V^2} \frac{f_{s,WOP}}{f_s}}, \quad (A18)$$

which completes the derivation for the noise signal strength to be added to WOP signal.

375 The instrument noise added to the WOP signals assumed the SNR of a MetOp-A occultation as the reference in (A18). The measurement is part of an end-of-life experimental campaign performed by EUMETSAT (European Organization for the Exploitation of Meteorological Satellites), where the vertical coverage of GRAS instrument was extended temporarily up to 600 km (originally ~ 80 km). Fig. A1 shows L1 C/A SNR of the occultation event scaled to $f_s = 1$ Hz, which was not affected by ionospheric disturbances ($S_4 \leq 0.2$), and the WOP amplitude with added noise on the last PS.

380 In our WOP simulations, the GNSS signal is propagated up to the rightmost PS. In order to define $f_{s,WOP}$ in this particular scenario, the scanning velocity in the horizontal direction was approximate to $v_s = 3.2$ km/s. Given the number of points per PS (2×10^{18}) and screen height (1000 km), the WOP sampling frequency in (A18) is $f_{s,WOP} = 839$ Hz.

The S_4 index presented throughout the evaluations includes the added instrument noise. Thus (Syndergaard, 2006),

$$S_4 = \frac{\sqrt{\langle (I - \bar{I})^2 \rangle}}{\bar{I}}, \quad (A19)$$

385 where the signal intensity $I \propto |\hat{u}_{total} \hat{u}_{total}^*|$, \bar{I} stands for the filtered intensity and $\langle \rangle$ correspond to 10-s average.

Author contributions. VLB, JR and TS designed the study cases and VLB performed the simulations and processing. VLB prepared the manuscript with contributions from all co-authors. JR prepared the Appendix.

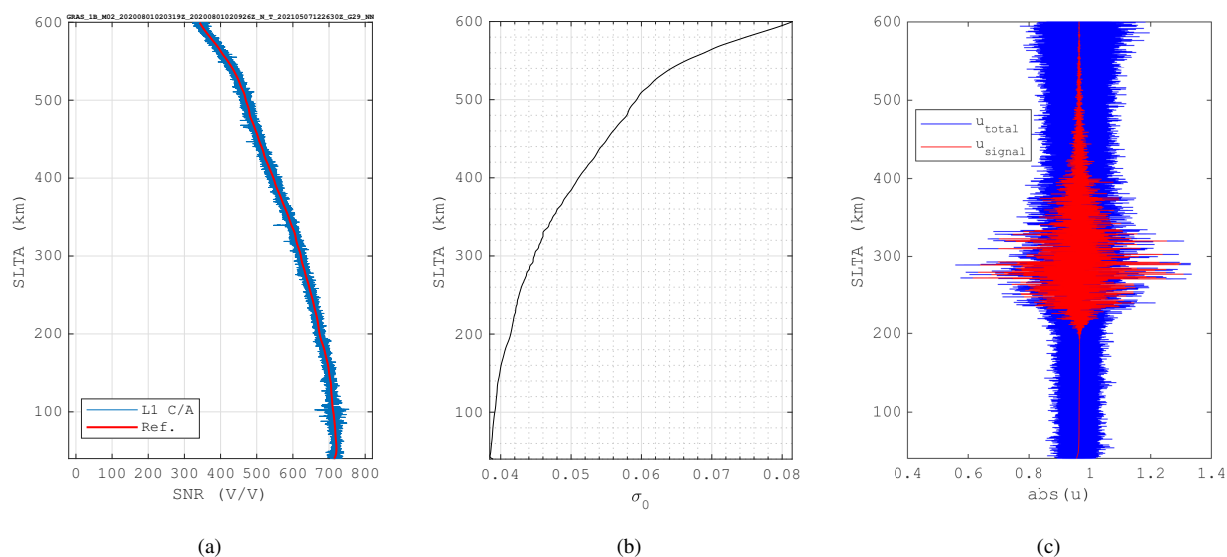


Figure A1. (a) L1 C/A $\text{SNR}_{1\text{Hz}}$: Blue curve shows the original SNR and red curve depicts the averaged curve which values were used as reference in (A18). The decay in SNR observed with increasing SLTA (> 100 km) is due to the antenna gain pattern. (b) Amplitude of the noise added to the WOP signal. (c) WOP amplitude with and without added noise on the observational plane (last PS), single inbound bubble scenario (Carrano et al., 2011).

Competing interests. The authors declare that they have no conflict of interest.

Acknowledgements. This research was supported by National Space Engineering Program (NRFP-4), funded by Swedish National Space Agency (Rymdstyrelsen). The authors would like to thank Riccardo Notarpietro (EUMETSAT) for sharing the data of GRAS ionospheric extension experiment on EPS MetOp-A, which was used as reference in this work.



References

- Aarons, J.: Global morphology of ionospheric scintillations, *Proceedings of the IEEE*, 70, 360–378, <https://doi.org/10.1109/PROC.1982.12314>, 1982.
- 395 Arras, C. and Wickert, J.: Estimation of ionospheric sporadic E intensities from GPS radio occultation measurements, *Journal of Atmospheric and Solar-Terrestrial Physics*, 171, 60–63, <https://doi.org/10.1016/j.jastp.2017.08.006>, 2018.
- Bevis, M., Businger, S., Herring, T. A., Rocken, C., Anthes, R. A., and Ware, R. H.: GPS meteorology: Remote sensing of atmospheric water vapor using the global positioning system, *Journal of Geophysical Research*, 97, 15 787, <https://doi.org/10.1029/92JD01517>, 1992.
- Carrano, C. S., Groves, K. M., Caton, R. G., Rino, C. L., and Straus, P. R.: Multiple phase screen modeling of ionospheric scintillation along
400 radio occultation raypaths, *Radio Science*, 46, 1–14, <https://doi.org/10.1029/2010RS004591>, 2011.
- Cherniak, I., Zakharenkova, I., and Sokolovskiy, S.: Multi-Instrumental Observation of Storm-Induced Ionospheric Plasma Bubbles at Equatorial and Middle Latitudes, *Journal of Geophysical Research: Space Physics*, 124, 1491–1508, <https://doi.org/10.1029/2018JA026309>, 2019.
- Culverwell, I. D. and Healy, S. B.: Simulation of L1 and L2 bending angles with a model ionosphere, Tech. Rep. 17, Danish Meteorological
405 Institute, Copenhagen, http://www.romsaf.org/general-documents/rsr/rsr_17.pdf, 2015.
- Dahl Mortensen, M.: The Back-Propagation Method for Inversion of Radio Occultation Data, Tech. Rep. 14, Danish Meteorological Institute, Copenhagen, Denmark, <https://www.dmi.dk/fileadmin/Rapporter/SR/sr98-14.pdf>, 1998.
- Fjeldbo, G., Kliore, A. J., and Eshleman, V. R.: The Neutral Atmosphere of Venus as Studied with the Mariner V Radio Occultation Experiments, *The Astronomical Journal*, 76, 123, <https://doi.org/10.1086/111096>, 1971.
- 410 Gorbunov, M. and Gurvich, A. S.: Microlab-1 experiment: Multipath effects in the lower troposphere, *Journal of Geophysical Research: Atmospheres*, 103, 13 819–13 826, <https://doi.org/10.1029/98JD00806>, 1998a.
- Gorbunov, M. and Gurvich, A. S.: Algorithms of inversion of microlab-1 satellite data including effects of multipath propagation, *International Journal of Remote Sensing*, 19, 2283–2300, <https://doi.org/10.1080/014311698214721>, 1998b.
- Gorbunov, M. E. and Lauritsen, K. B.: Linearized Zverev Transform and its application for modeling radio occultations, *Radio Science*, 42,
415 <https://doi.org/10.1029/2006RS003590>, 2007.
- Gorbunov, M. E., Gurvich, A. S., and Shmakov, A. V.: Back-propagation and radio-holographic methods for investigation of sporadic ionospheric E-layers from Microlab-1 data, *International Journal of Remote Sensing*, 23, 675–685, <https://doi.org/10.1080/01431160010030091>, 2002.
- Healy, S. B. and Culverwell, I. D.: A modification to the standard ionospheric correction method used in GPS radio occultation, *Atmospheric
420 Measurement Techniques*, 8, 3385–3393, <https://doi.org/10.5194/amt-8-3385-2015>, 2015.
- Jiao, Y. and Morton, Y. T.: Comparison of the effect of high-latitude and equatorial ionospheric scintillation on GPS signals during the maximum of solar cycle 24, *Radio Science*, 50, 886–903, <https://doi.org/10.1002/2015RS005719>, 2015.
- Kelley, M. C., Larsen, M. F., LaHoz, C., and McClure, J. P.: Gravity wave initiation of equatorial spread F: A case study, *Journal of Geophysical Research*, 86, 9087, <https://doi.org/10.1029/JA086iA11p09087>, 1981.
- 425 Kelly, M. A., Comberiate, J. M., Miller, E. S., and Paxton, L. J.: Progress toward forecasting of space weather effects on UHF SATCOM after Operation Anaconda, *Space Weather*, 12, 601–611, <https://doi.org/10.1002/2014SW001081>, 2014.



- Kepkar, A., Arras, C., Wickert, J., Schuh, H., Alizadeh, M., and Tsai, L.-c.: Occurrence climatology of equatorial plasma bubbles derived using FormoSat-3/COSMIC GPS radio occultation data, *Annales Geophysicae*, 38, 611–623, <https://doi.org/10.5194/angeo-38-611-2020>, 2020.
- 430 Knepp, D.: Multiple phase-screen calculation of the temporal behavior of stochastic waves, *Proceedings of the IEEE*, 71, 722–737, <https://doi.org/10.1109/PROC.1983.12660>, 1983.
- Kursinski, E. R., Hajj, G. A., Schofield, J. T., Linfield, R. P., and Hardy, K. R.: Observing Earth's atmosphere with radio occultation measurements using the Global Positioning System, *Journal of Geophysical Research: Atmospheres*, 102, 23 429–23 465, <https://doi.org/10.1029/97JD01569>, 1997.
- 435 Liu, C., Kirchengast, G., Syndergaard, S., Schwaerz, M., Danzer, J., and Sun, Y.: New higher-order correction of GNSS-RO bending angles accounting for ionospheric asymmetry: Evaluation of performance and added value, *Remote Sensing*, 12, 1–23, <https://doi.org/10.3390/rs12213637>, 2020.
- Sokolovskiy, S., Schreiner, W., Rocken, C., and Hunt, D.: Detection of high-altitude ionospheric irregularities with GPS/MET, *Geophysical Research Letters*, 29, <https://doi.org/10.1029/2001GL013398>, 2002.
- 440 Sommerfeld, A.: *Optics: Lectures on Theoretical Physics*, Vol. IV, Academic Press Inc., New York, USA, 4th edn., 1967.
- Stolle, C., Lühr, H., Rother, M., and Balasis, G.: Magnetic signatures of equatorial spread F as observed by the CHAMP satellite, *Journal of Geophysical Research*, 111, A02 304, <https://doi.org/10.1029/2005JA011184>, 2006.
- Stolle, C., Lühr, H., and Fejer, B. G.: Relation between the occurrence rate of ESF and the equatorial vertical plasma drift velocity at sunset derived from global observations, *Annales Geophysicae*, 26, 3979–3988, <https://doi.org/10.5194/angeo-26-3979-2008>, 2008.
- 445 Syndergaard, S.: COSMIC S4 Data, https://cdaac-www.cosmic.ucar.edu/cdaac/doc/documents/s4_description.pdf, 2006.
- Vorob'ev, V. V. and Krasil'nikova, T. G.: Estimation of the accuracy of the atmospheric refractive index recovery from doppler shift measurements at frequencies used in the NAVSTAR system, *USSR Phys. Atmos. Ocean, Engl. Transl.*, 29, 602–609, 1994.
- Wickert, J., Pavelyev, A. G., Liou, Y. A., Schmidt, T., Reigber, C., Igarashi, K., Pavelyev, A. A., and Matyugov, S. S.: Amplitude variations in GPS signals as a possible indicator of ionospheric structures, *Geophysical Research Letters*, 31, L24 801, <https://doi.org/10.1029/2004GL020607>, 2004.
- 450 Xiong, C., Stolle, C., Lühr, H., Park, J., Fejer, B. G., and Kervalishvili, G. N.: Scale analysis of equatorial plasma irregularities derived from Swarm constellation, *Earth, Planets and Space*, 68, <https://doi.org/10.1186/s40623-016-0502-5>, 2016.
- Yeh, K. and Liu, C.-H.: Radio wave scintillations in the ionosphere, *Proceedings of the IEEE*, 70, 324–360, <https://doi.org/10.1109/PROC.1982.12313>, 1982.
- 455 Zeng, Z. and Sokolovskiy, S.: Effect of sporadic E clouds on GPS radio occultation signals, *Geophysical Research Letters*, 37, 1–5, <https://doi.org/10.1029/2010GL044561>, 2010.
- Zeng, Z., Sokolovskiy, S., Schreiner, W. S., and Hunt, D.: Representation of Vertical Atmospheric Structures by Radio Occultation Observations in the Upper Troposphere and Lower Stratosphere: Comparison to High-Resolution Radiosonde Profiles, *Journal of Atmospheric and Oceanic Technology*, 36, 655–670, <https://doi.org/10.1175/JTECH-D-18-0105.1>, 2019.